Complete state tomography of a quantum dot spin qubit

Dan Cogan ⬤, Giora Peniakov ⬤, Zu-En Su, and David Gershoni ⬤*

Physics Department and Solid State Institute, Technion–Israel Institute of Technology, 3200003 Haifa, Israel

Semiconductor quantum dots are probably the preferred choice for interfacing anchored matter spin qubits and flying photonic qubits. While full tomography of a flying qubit or light polarization is, in general, straightforward, matter spin tomography is a challenging and resource-consuming task. Here we present an all-optical method for conducting full tomography of quantum dot confined spins. Our method is applicable for electronic spin configurations such as the conduction-band electron and the valence-band hole and for electron-hole pairs such as the bright and dark excitons. We excite the spin qubit using a short, resonantly tuned, polarized optical pulse, which coherently converts the qubit to an excited qubit that decays by emitting a polarized single photon. We perform the tomography by using two different orthogonal, linearly polarized excitations, followed by time-resolved measurements of the degree of circular polarization of the emitted light from the decaying excited qubit. We demonstrate our method on the dark exciton spin state with a fidelity of 0.94, mainly limited by the accuracy of our polarization analyzers.

I. INTRODUCTION

Qubits are the building blocks of quantum technologies [1,2]. Qubits can be realized in many physical two-level systems, which maintain their coherence for a much longer time than the time required to initialize their coherent states, read, or subject the state to logical gates [3–6]. The vision of quantum technologies is frequently described in terms of anchored qubits, located on different nodes in space where they serve as quantum information processors or quantum memories, and flying qubits that propagate long distances, connecting the various nodes[7]. Photons are natural flying qubits since they can travel long distances without dephasing, while their polarization state carries the quantum information [8,9]. The spins of single electrons, nuclei, atoms, and molecules are examples for anchored qubits. In some instances, they can be isolated, thereby maintaining spin coherence for very long times [4,10–13]. Semiconductor quantum dots are an excellent interface between anchored spin qubits and flying photonic qubits due to their ability to both isolate electronic spin qubits and to enhance their interaction with the photons' light field. Quantum photonic devices based on semiconductor quantum dots, such as that described in Fig. 1(a), are almost ideally suited for building high-performing, optically active quantum nodes.

Determining the qubit state generally requires projections on various basis states in a process called tomography. Full tomography of the polarization state of flying photonic qubits is quite straightforwardly done using state-of-the-art polarizers and retarders [14,15]. Researchers have developed methods for measuring matter qubits' spin in various systems [16–22]. Optically, this task can be straightforward if the matter qubit's two states form an optical Λ-system with one auxiliary level.

An example of such a system realized in quantum dots (QDs) is the all-optical method developed by Benny *et al.* [23], demonstrating full tomography of a QD confined bright exciton (BE; an electron-hole pair) spin. The bright exciton is formed by absorption of a photon which excites an electron from the full valence band to the empty conduction band. In this process the photon does not affect the electron spin. The absorbed photon angular momentum is preserved in the optical transition since the electron in the valence band has one unit of atomic orbital momentum, while in the conduction band its orbital momentum vanishes. The missing valence-band electron can be regarded as a hole which pairs with the electron in forming a BE with a total angular projection of either $+1$ or -1 on the QD symmetry axis, depending on the circular polarization of the absorbed photon. This BE spin qubit forms an optical Λ system with the total spin-zero biexciton state, which results from resonant optical excitation of the BE, as schematically described in Fig. 1(b). In the Λ system, each of the BE qubit's states is optically connected to the biexciton single state. This facilitate a relatively easy method for optical spin tomography [23] and coherent spin control [24] resulting from a one-to-one correspondence between the polarization of the spin and the photon, inducing the optical transition.

The situation is different for a QD confined single-charge carrier such as the conduction-band electron or the valence-band hole. Such a carrier has a half-integer spin. As such, it can never form an optical Λ system with one nondegenerate auxiliary level. Instead, it always forms an optical Π system with its excited charge carrier qubit states: The positive or negative trions. The confined spin qubit and the optically excited one are both spin qubits that form an optical Π system, as can be seen in Fig. 1(c). The conduction-band electron [1,2,25], the valence-band hole [26,27], and the dark exciton (DE; optically inactive electron-hole pair) [28–30] are long-lived ground electronic spin qubits in a QD system.
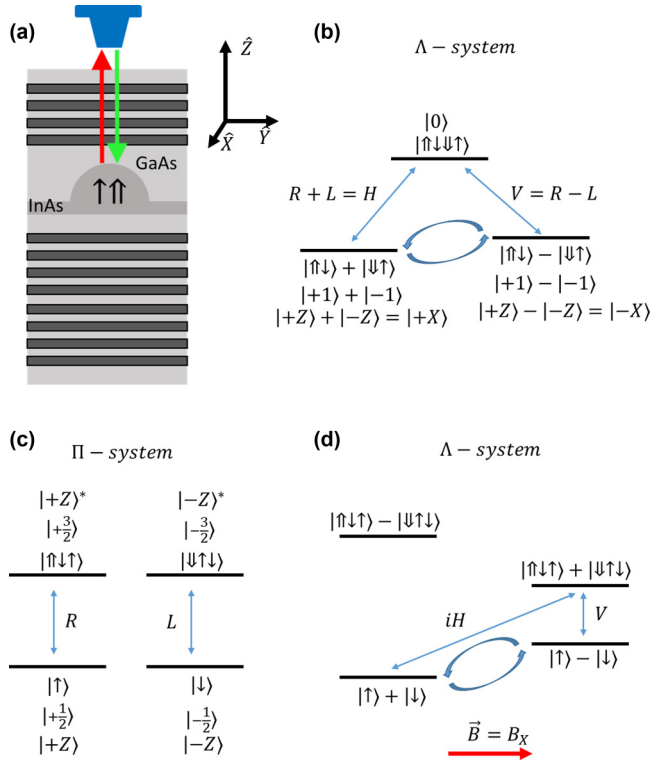
*dg@physics.technion.ac.il

FIG. 1. (a) Schematic description of the studied single-QD device. The QD is located in the focal point of a microscope objective, which focuses the pulsed laser beams (represented by a green arrow) and collimates the emitted PL (red arrow). Here $\hat{z}$ defines the growth direction and the symmetry axis of the QD. (b) Schematic description of the confined BE-biexciton as an optical Λ system and (c) the confined electron-trion as an optical Π system. (d) Transformation of an optical Π system into an artificial L system using an external magnetic field. Here $\uparrow$ ($\Downarrow$) represents the spin-up electron (spin-down hole), and R and L represent right- and left-hand circularly polarized optical transitions. Numbers indicate the total angular momentum of the electronic state, and $|+Z\rangle$ $(|-Z\rangle^*)$ represents the spin-up ground (spin-down excited) state along the $\hat{z}$ axis. Thus, $|+X\rangle$ $(|-X\rangle^*)$ represents coherent superpositions as defined.

All three qubits form a natural Π system with circularly polarized optical selection rules for their excited qubits [13], and therefore, tomography as in the BE case [23] is impossible for these spin qubits.

One way to circumvent this problem, as described in Fig. 1(d), is to apply a strong magnetic field, which lifts the Kramers degeneracy of the optically excited spin state, thereby facilitating an optical Λ-like system between the carrier's spin states and one of the optically excited states [31–33]. However, the strong magnetic field also lifts the degeneracy of the ground-level qubit, thus creating spectral "which-path" information for the emitted photons. Therefore, the use of this artificially created Λ system for spin-photon entanglement [33–35] requires erasing the spectral or polarization information encoded in the emitted photon, thereby limiting the method applicability and scalability.

Here we develop and demonstrate an all-optical spin tomography method which uses the natural Π system that the spin qubit is a part of for the optical tomography. The method is general and accurate and can be applied for state tomography of multiqubits and entangled spin-multiphoton states [36–38]. We perform the tomography in the following way: first, we excite the spin qubit under study, which we call the ground-level qubit, to an optically active excited qubit state, which we call the excited qubit. This coherent and deterministic conversion is done using a short, resonantly tuned, linearly polarized optical π pulse, such that there is a one-to-one correspondence between the state of the ground-level qubit and that of the excited qubit. The excited qubit then radiatively recombines while its spin state evolves during the recombination on a frequency given by the energy difference between the excited qubit eigenstates. The Π-system optical selection rules are such that by using time-resolved circular-polarization-sensitive photoluminescence (PL) spectroscopy one can trace back the state of the excited qubit at the moment of conversion and, in turn, the state of the ground-level qubit, prior to the conversion pulse. Full tomography is obtained using two conversions on two different linear polarization bases.

We note, however, that for the Kramers degenerate spin qubits, a minimal external magnetic field in the Voigt configuration is still required to lift the excited-qubit degeneracy and thereby induce spin precession. The energy difference between the qubits' eigenstates is kept, in this case, much smaller than the radiative spectral width, thereby avoiding spectral which-path information to be carried with the emitted photons.

Although our optical tomography method applies to single-charge carriers, we prefer to demonstrate it using the DE. We do that for two reasons:

(i) The DE and its excited biexcitonic spin qubit (BIE) are integer spin qubits, and even in the absence of external magnetic field, the exchange interactions between the carriers remove the degeneracy between their spin-up and spin-down states [28,39,40]. Their eigenstates are described by $|\pm X_{DE}\rangle = (|+Z_{DE}\rangle \pm |-Z_{DE}\rangle)/\sqrt{2}$ and $|\pm X_{BIE}\rangle = (|+Z_{BIE}\rangle \pm |-Z_{BIE}\rangle)/\sqrt{2}$. The energy differences between the eigenstates are of the order of 1 μeV which is smaller than the radiative width of the BIE optical transition ($\simeq 3$ μeV) and much smaller than the spectral width of our laser pulse ($\simeq 100$ μeV). Due to these splittings, the DE and BIE precession times around the eigenstates' axis, T_{DE} and T_{BIE}, are about an order of magnitude longer than the radiative time of the BIE.

(ii) Due to a small mixture between the BE and DE states, it is possible to initialize the DE spin state with high fidelity using a single optical pulse [30], just like the BE [23]. Initialization of the electron or hole spin state is much more complicated [16,41,42].

Another useful feature of the DE system is that the excitation and emission of the BIE occur at different wavelengths [28], preventing the laser light from blinding the PL detectors.

II. THE TOMOGRAPHY METHOD

The typical size of an epitaxially grown semiconductor QD is tens of nanometers in diameter and a few nanometers in height, forming a three-dimensional potential trap that
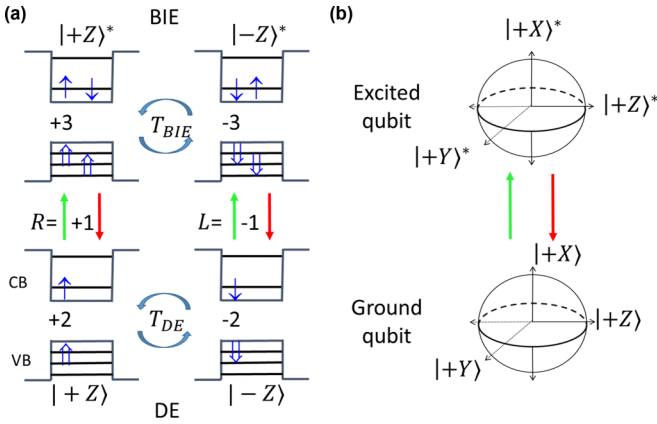
FIG. 2. (a) Energy levels, spin wave functions, and polarization selection rules for resonant optical transitions for the QD confined dark exciton (DE) and the optical Π system that it forms with its optically excited biexciton (BIE). (b) Bloch sphere representation of the confined ground spin qubit and the excited spin qubit. Here $|+Z\rangle$ $(|-Z\rangle^*)$ represents the spin-up ground (spin-down excited) state along the $\hat{z}$ axis, and $|+X\rangle$ $(|-X\rangle^*)$ and $|+Y\rangle$ $(|-Y\rangle^*)$ represent coherent superpositions.

confines electrons, holes, and electron-hole pairs (excitons). Figure 1(a) illustrates the QD device used in this work. The InAs layer of the QDs is embedded in a GaAs optical microcavity formed by two Bragg reflecting mirrors of AlGaAs/GaAs. The role of the microcavity is to increase the harvesting efficiency of the light emitted from the QD [43]. A microscope objective with a numerical aperture of 0.8 is used both to focus the laser pulses on a single QD and to collect the single photons emitted.

A QD confined DE is composed of a conduction-band electron and a valence-band hole pair, with parallel spins [28,29]. It is called dark since the two carriers cannot recombine radiatively due to their electronic spin mismatch. This fact is also reflected in the DE total angular momentum projection of ± 2, which cannot be carried out by a single photon possessing an angular momentum of only ± 1. Consequently, the QD confined DE forms a spin qubit which has orders of magnitude longer lifetime than the BE [29,44].

The DE can be optically excited by absorbing a photon, thereby photogenerating an additional electron-hole pair in the QD. Resonant excitation of the DE as schematically described in Fig. 2(a) will result in a BIE. The relevant absorption spectrum which presents this absorption spectral line is given in Fig. 8(c) of Ref. [45]. The BIE is a four-carrier state composed of two antiparallel electron spins forming a singlet in the lowest conduction-band level and two heavy holes with parallel spins, forming a triplet, where one hole is in the valence band's ground energy level and the other one is in the first excited energy level. The total angular momentum of the BIE is ± 3, given by the total spin projection of the two unpaired holes. Figure 2(b) illustrates the Bloch sphere representation of the confined ground spin qubit and the excited spin state. $|+Z\rangle$ $(|-Z\rangle^*)$ represents the spin-up ground (spin down excited) state along the $\hat{z}$ axis, defined by the growth direction of the QD, and $|+X^*\rangle$ $(|-X\rangle^*)$ and $|+Y\rangle$ $(|-Y\rangle^*)$ represent coherent superpositions, as illustrated

in Fig. 2(b). We note that the $|\pm X^*\rangle$ states are the excited qubit eigenstates, split in energy by about 1 μeV due to the hole-hole anisotropic exchange interaction [46]. After photogeneration, within its radiative lifetime of $\tau_R = 0.39 \pm 0.01$ ns, the excited spin decays by emitting a photon. One notes in Figs. 1(c) and 2(b) that the ground and excited qubits form an optical Π system, in which right- (left-) hand circularly polarized optical transitions connect the $|+Z\rangle (|-Z\rangle)$ states of the ground and excited qubits.

We use a linearly polarized resonant optical π pulse to convert the ground qubit coherently and deterministically to the excited qubit, with a one-to-one correspondence between the two states. The excited qubit then radiatively decays while its spin state evolves with a precession time of $T_{\text{BIE}} = 5.70 \pm 0.05$ ns during the relaxation. The selection rules of the optical Π system are such that a spin-up state of the excited qubit $(|Z\rangle^*)$ results in the emission of a right-hand $(|R\rangle)$ circularly polarized photon, while a spin-down state $(|-Z\rangle^*)$ results in the emission of a left-hand $(|L\rangle)$ circularly polarized photon. Thus, by using time-resolved circularly polarized sensitive PL spectroscopy one can trace back the state of the excited qubit at the moment of conversion and, in turn, the state of the ground-level qubit prior to the conversion.

Figure 3 describes the procedure for full state tomography. The central Bloch sphere describes a general ground-level-qubit state as a coherent superposition of the two $|\pm Z\rangle$ states. Likewise, the outer Bloch spheres describe the states of the excited qubit as a superposition of the $|\pm Z^*\rangle$ states, following the optical pulse conversions, for four different pulse polarizations.

In Fig. 3, as in Fig. 2, the green arrow describes the π pulse which converts the ground-level qubit to the excited qubit, while the red arrow describes the single-photon emission resulting from the excited-qubit recombination. The ground spin state in Fig. 3 is defined on the central Bloch sphere by the vector

$$\overrightarrow{S}^0 = \left[S_X^0, S_Y^0, S_Z^0\right].$$

$\overrightarrow{S}^0$ is the spin state that one measures by state tomography. This state is converted to the excited qubit by applying a polarized 12-ps-long pulse, energetically tuned to the ground-level–excited-level optical transition. Since in this Π system $|R\rangle$ photons connect only between $|+Z\rangle$ and $|+Z^*\rangle$ states, while $|L\rangle$ photons connect only between $|-Z\rangle$ and $|-Z^*\rangle$ states, it follows that right- (left-) circularly polarized conversion pulse, successfully applied to the ground-level qubit, results in an excited qubit initial state which is given by $\overrightarrow{S}_*^{0,R(L)} = [0, 0, \pm 1]$, as shown in Fig. 3(a) [Fig. 3(b)]. Successful absorption of one of these two circularly polarized conversion pulses always initializes the excited qubit to the same states no matter what the ground-level-qubit state was prior to the conversion pulse. However, when the conversion pulses are linearly polarized, the situation is different. A $|H\rangle = 1/\sqrt{2}(|R\rangle + |L\rangle)$ polarized pulse converts the ground-spin state to the same excited-spin state, and a $|B\rangle = 1/\sqrt{2}\exp(-i\pi/4)(|R\rangle + i|L\rangle)$ linearly polarized pulse also rotates the excited-spin phase by $90°$ around the z axis, upon conversion. Thus, after H conversion, the initial state of
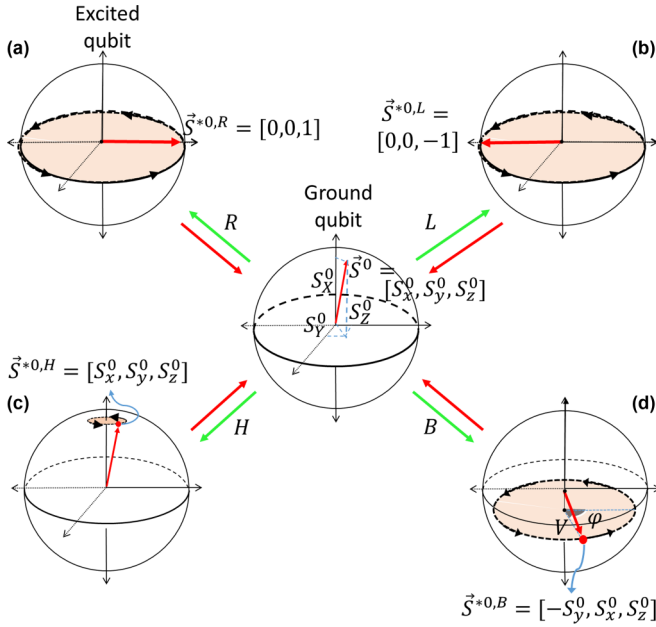
FIG. 3. Schematic description of the spin-state tomography. The red arrow on the central Bloch sphere represents the confined ground-level spin state, described by the vector $\vec{S}^0 = [S_X^0, S_Y^0, S_Z^0]$. A polarized optical π pulse (green arrow) converts the ground spin qubit into the excited qubit. The excited qubit evolves in time while it radiatively recombines and emits a single photon (red arrow). (a)–(d) describe four different polarizations of the converting pulse: (a) R conversion, (b) L conversion, (c) H conversion, and (d) B conversion. In each case, the red arrow on the excited-qubit Bloch sphere describes the excited-qubit state at the moment of conversion and the direction of the state's precession. The amplitude V^0 and the time-dependent phase $\varphi(t)$ characterize this precession. While R (L) circularly polarized excitation initializes the excited qubit in its $|+Z\rangle$ ($|-Z\rangle$) spin state, H (B) polarized excitation maintains the phase information of the ground qubit and converts it to $\vec{S}^{*0,H} = [S_X^0, S_Y^0, S_Z^0]$ ($\vec{S}^{*0,B} = [-S_Y^0, S_X^0, S_Z^0]$).

the excited qubit is given by

$$\vec{S}_*^{0,H} = \left[S_X^0, S_Y^0, S_Z^0\right], \tag{1}$$

as shown in Fig. 3(c), and after B conversion, the initial state is

$$\vec{S}_*^{0,B} = \left[-S_Y^0, S_X^0, S_Z^0\right], \tag{2}$$

as shown in Fig. 3(d).

Following the conversion, the initial excited-qubit state evolves in time by precessing around the eigenstate axis (X) with a time period T_{BIE}. The precessing state projection on the Z axis of the excited-qubit Bloch sphere is therefore given by

$$S_Z^*(t) = V^0 \cos\left(-\frac{2\pi t}{T_{\text{BIE}}} + \varphi^0\right), \tag{3}$$

where V^0 and φ^0 are the excited qubit's initial amplitude and phase. For R conversion

$$V^0 = V_R^0 = 1, \quad \varphi^0 = \varphi_R^0 = 0, \tag{4}$$

and for L conversion

$$V^0 = V_L^0 = 1, \quad \varphi^0 = \varphi_L^0 = \pi, \tag{5}$$

while for H conversion

$$V^0 = V_H^0 = \sqrt{(S_Y^0)^2 + (S_Z^0)^2}, \quad \varphi^0 = \varphi_H^0 = \arctan(S_Y^0/S_Z^0) \tag{6}$$

and for B conversion

$$V^0 = V_B^0 = \sqrt{(S_X^0)^2 + (S_Z^0)^2}, \quad \varphi^0 = \varphi_B^0 = \arctan(S_X^0/S_Z^0). \tag{7}$$

In addition to the natural coherent precession, the excited qubit undergoes decoherence [13,47], which results in decay of the initial precession amplitude:

$$V_p(t) = V_P^0 \exp\left(-t^2/T_2^{*2}\right), \tag{8}$$

where $P = R, L, H$, or B and T_2^* is the dephasing time of the excited qubit. In addition, the excited qubit decays radiatively, while its spin state precesses. Its PL emission intensity as a function of time is given by

$$I(t) = I^0 \exp(-t/\tau_R), \tag{9}$$

where τ_R is its radiative lifetime and I^0 is the initial emission intensity.

These three processes of Eqs. (3)–(9) happen simultaneously, and thus, the time-dependent circularly polarized PL intensity of the excited qubit can be described by

$$I_R(t) = I^0 \exp(-t/\tau_R)$$
$$\times \left[1 + V^0 \exp\left(-t^2/T_2^{*2}\right) \cos\left(-\frac{2\pi t}{T_{\text{excited}}} + \varphi^0\right)\right] \Big/ 2 \tag{10}$$

and

$$I_L(t) = I^0 \exp(-t/\tau_R)\left[1 + V^0 \exp\left(-t^2/T_2^{*2}\right)\right.$$
$$\left. \times \cos\left(-\frac{2\pi t}{T_{\text{excited}}} + \varphi^0 + \pi\right)\right] \Big/ 2 \tag{11}$$

for right- and left-circularly polarized PL emission, respectively.

The time-dependent DCP is defined as $\text{DCP}(t) = [I_R(t) - I_L(t)]/[I_R(t) + I_L(t)]$; therefore, it is given by

$$\text{DCP}_p(t) = V_P^0 \exp(-t^2/T_2^{*2}) \cos\left(-\frac{2\pi t}{T_{\text{excited}}} + \varphi_P^0\right). \tag{12}$$

Since T_{BIE} and T_2^{*2} can be measured independently (see below), one can quite accurately obtain the four variables V_H^0, V_B^0, φ_H^0, and φ_B^0 by fitting Eq. (12) to the measured time-dependent $\text{DCP}_p(t)$ resulting from the two converting pulses. These four variables accurately define the initial ground-level-qubit spin state as described by the three projections $[S_X^0, S_Y^0, S_Z^0]$ using Eqs. (6) and (7).

III. EXPERIMENT

In Fig. 4 we schematically describe the experimental system. The system operates as follows: The first 7-ns-long optical pulse (magenta) depletes the QD from charges and
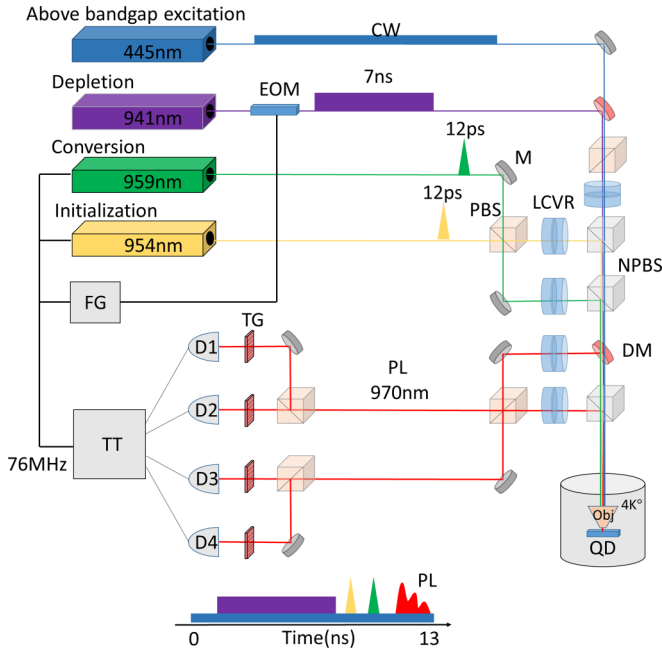
FIG. 4. Schematic description of the experimental setup. PBS, polarizing beam splitter; NPBS, nonpolarizing beam splitter; M, mirror; DM, dichroic mirror; TT, time tagger; TG, transmission grating; OBJ, microscope objective; QD, quantum dot device; PL, collected PL emission; LCVR, liquid-crystal variable retarder; Dn, superconducting single-photon detector n; CW, continuous wave; FG, function generator; EOM, electro-optic modulator. The bottom panel describes the sequence of pulses and PL emission during one cycle of the repeated experiment at 76 MHz.

from the remaining DE. The depletion procedure is described elsewhere [48]. We then write the DE spin state using an adequately polarized 12-ps optical π pulse (yellow) to an excited DE state. The initialization procedure is discussed in detail in Ref. [30]. The main inaccuracy in the initialization is due to incomplete depletion of the QD from the DE, which remains from the previous period. This leaves a thermal DE population of about 18%, which is accurately measured using time-resolved PL measurements [48]. In addition, there are other sources of uncertainty, which are due to the finite accuracy of the liquid-crystal variable retarders, which we carefully characterize to be less than 5% [13]. About 100 ps later, after the excited DE relaxes to its ground level, a third, linearly polarized 12-ps optical π pulse (green) converts the DE into the BIE. The resulting PL emission (red) is then projected on two orthogonal circular polarizations and detected using four superconducting single-photon counters. The obtained time-resolved degree of circular polarization concludes the DE spin state tomography. This cycle is repeated at a 76-MHz rate.

Figure 5 describes the measurements used to characterize the BIE as a spin qubit. For these measurements the DE is prepared in a thermal, totally mixed unpolarized state using a feeble continuous-wave above-band-gap excitation (457 nm) of the QD [13,49]. A 12-ps-long resonantly tuned laser pulse then excites the DE to form a BIE. We use three different polarizations for the pulsed excitation: $|R\rangle$, $|L\rangle$, and $|H\rangle$. Since the DE-BIE is an optical P system, the R (L) polarized pulse initializes the BIE in the $|+Z_{\text{BIE}}\rangle$ ($|-Z_{\text{BIE}}\rangle$)
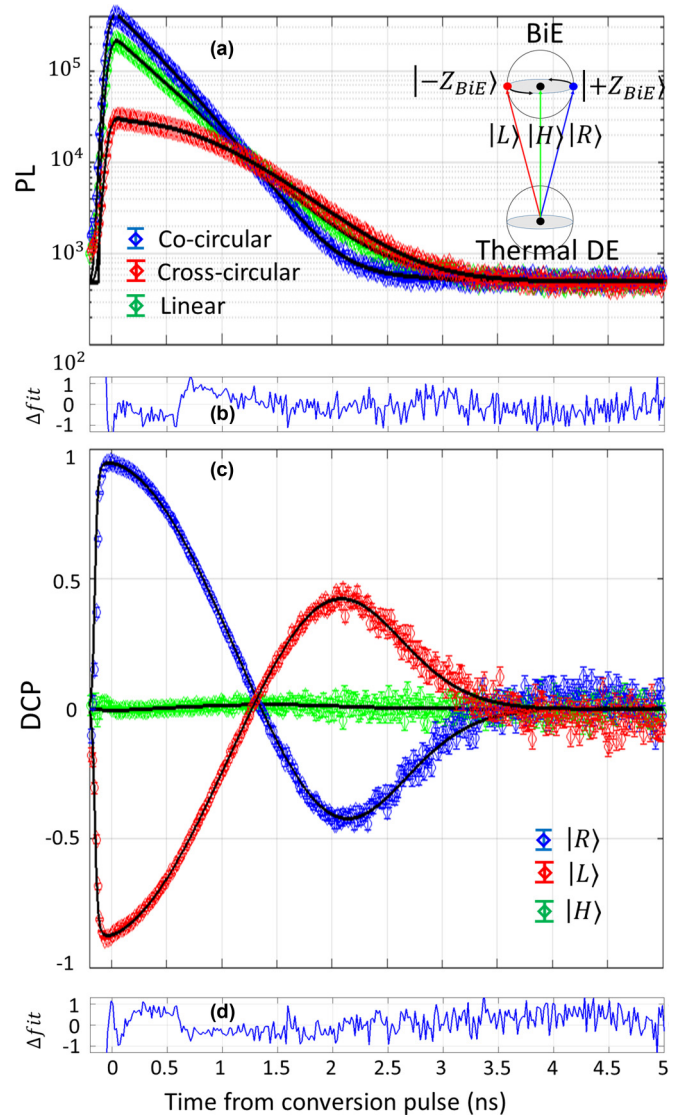

FIG. 5. Experimental characterization of the BIE (excited DE) spin qubit. (a) Polarization-sensitive time-resolved PL measurement of the recombining BIE spectral line, following polarized pulsed excitation. Blue (red) diamonds represent PL, detected in a cocircular (cross-circular) polarization to the polarization of the excitation, and green diamonds represent circularly polarized detection after linearly polarized excitation. The color-matched solid lines represent the best model fits to the data using Eqs. (10) and (11) with three fitting parameters: $T_{\text{BIE}} = 5.70 \pm 0.05$ ns, $T_2^* = 5.75 \pm 0.05$ ns, and $\tau_R = 0.39 \pm 0.01$ ns. (b) The difference between the fitted model and the measured cocircular polarization data normalized by the experimental uncertainty. (c) Time-resolved degree of circular polarization (DCP) of the PL for R, L, and H polarized excitations. (d) The difference between the fitted model and measured DCP for R excitation, normalized by the experimental uncertainty.

state, while the H polarized pulse results in a totally mixed BIE state. Following its photogeneration, the BIE evolves in time while it recombines radiatively. In Fig. 5(a), we present the measured circularly polarized PL as a function of time after the pulsed excitation for three different cases. The blue (red) diamonds present PL, polarized cocircular (cross circular) to the excitation pulse, and the green line presents

TABLE I. Tomography and measured rates.

State	S_X^0	S_Y^0	S_Z^0
$|+X_{DE}\rangle$	0.74 ± 0.03	-0.09 ± 0.02	0.09 ± 0.02
$|-X_{DE}\rangle$	-0.71 ± 0.03	-0.09 ± 0.02	0.12 ± 0.02
$|+Y_{DE}\rangle$	0.19 ± 0.03	0.78 ± 0.02	0.21 ± 0.02
$|-Y_{DE}\rangle$	-0.19 ± 0.03	-0.78 ± 0.02	0.04 ± 0.02
$|+Z_{DE}\rangle$	0.00 ± 0.03	-0.02 ± 0.03	0.82 ± 0.01
$|-Z_{DE}\rangle$	0.01 ± 0.03	-0.09 ± 0.03	-0.78 ± 0.01
Quantity	Symbol	Time (ns)	
DE precession period [28]	T_{DE}	3.1 ± 0.1	
BIE precession period	T_{BIE}	5.70 ± 0.05	
BIE dephasing time	T_2^*	5.75 ± 0.05	
BIE radiative lifetime	τ_R	0.39 ± 0.01	

PL polarized both R and L, following an H polarized pulse. The solid black lines present the best-fit model of Eqs. (10) and (11). For the R (L) circularly polarized conversion pulse the initial BIE phase φ^0 is 0 (π), and the visibility V^0 is 1 (1). For the linear initialization $V^0 = 0$. In the last case, the PL simply decays radiatively. Therefore, this measurement is
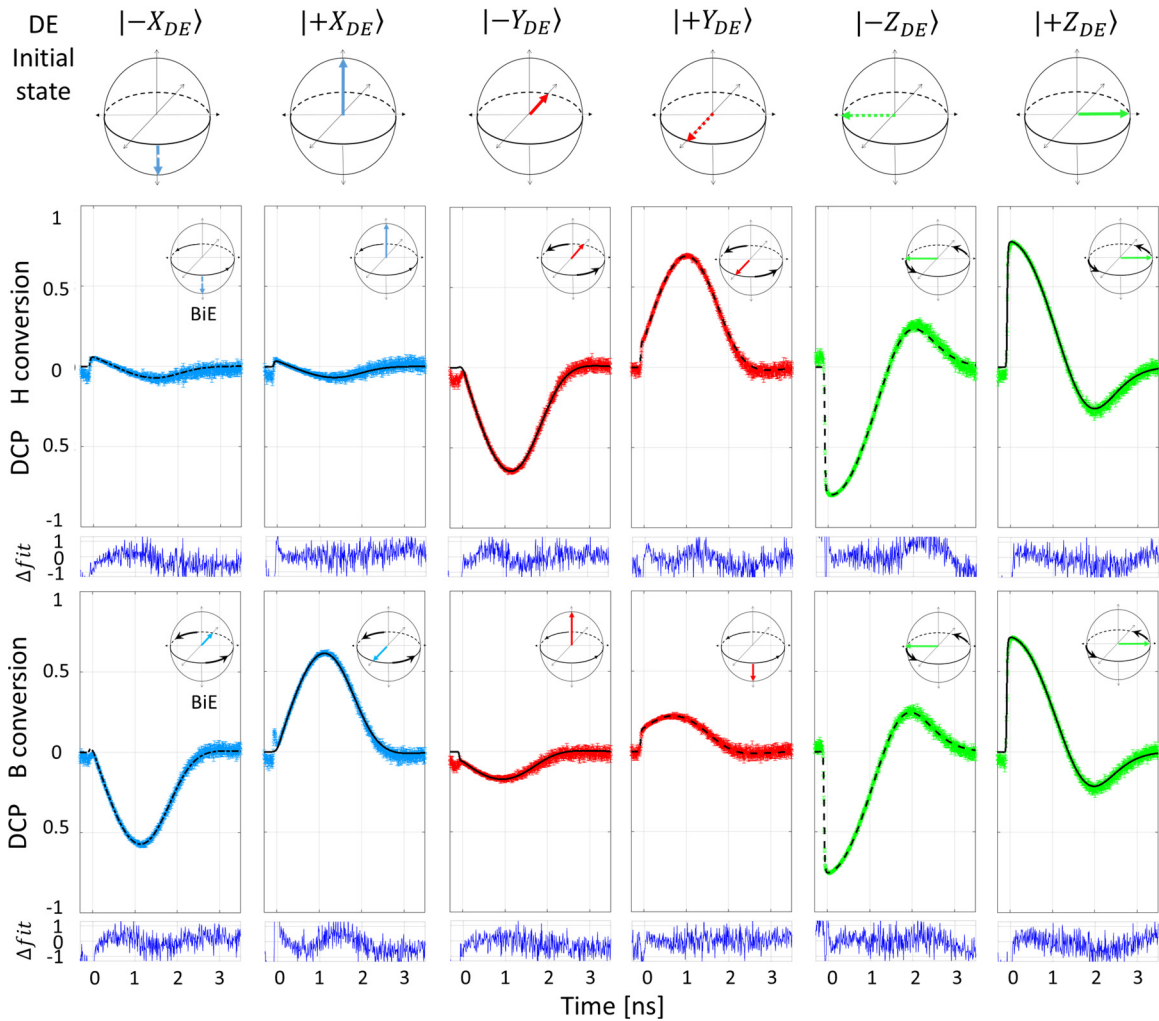

FIG. 6. Full state tomography of the confined DE spin state for six different DE initializations in three orthogonal bases. Blue, red, and green arrows describe $|\pm X_{DE}\rangle$, $|\pm Y_{DE}\rangle$, and $|\pm Z_{DE}\rangle$ initializations on the top DE Bloch spheres. Below each initialization's Bloch sphere, color-matched solid lines describe the measured time-resolved DCP(t) following H and B conversions. Overlaid solid black lines represent the best-fit model using Eq. (12) fitted to the measured data. The time-resolved differences between the fitted model and the measured DCP, normalized by the experimental uncertainty, are presented below each curve. The Bloch spheres in the insets describe the initial BIE spin state after the conversion and its temporal precession while it radiatively recombines.

used to determine the radiative lifetime without any additional fitting parameters. The BIE precession period and its dephasing are then fitted accurately using both the time-resolved PL measurements [$I_R(t)$ and $I_L(t)$] and DCP(t) as presented in Figs. 5(a) and 5(c), respectively. The measurements are fitted simultaneously, and we obtain $T_{\mathrm{BIE}} = 5.70 \pm 0.05$ ns, $T_2^* = 5.75 \pm 0.05$ ns, and $\tau_R = 0.39 \pm 0.01$ ns (see Table I). As can be seen in Figs. 5(b) and 5(d), our fitting procedure agrees with all the measured data points within one standard deviation of the experimental uncertainty.

Figure 6 displays the results of the tomographic measurements for which the DE is first initialized in a well-characterized state. In Fig. 6, each DE initialization is described by an arrow on the Bloch sphere on the top panel. $|\pm X_{\mathrm{DE}}\rangle$, $|\pm Y_{\mathrm{DE}}\rangle$, and $|\pm Z_{\mathrm{DE}}\rangle$ initializations are represented by blue, red, and green arrows, respectively. The color-matched solid lines below each initialization represent the measured DCP as a function of time after the conversion for both H and B conversions. Black solid lines overlaid on the measured DCP represent the best-fit model using Eq. (12). The differences between the fitted model and the measured DCP, normalized by the experimental uncertainty, are presented below each curve. The quality of the fits is evident since every measured point is within the experimental uncertainty of the calculated one. In the inset of each panel are schematic descriptions of the BIE spin state after the conversion pulse and its temporal evolution during its recombination.

IV. DISCUSSION

One notes that for the $|-X_{\mathrm{DE}}\rangle$ and $|+X_{\mathrm{DE}}\rangle$ initializations, the DCP for H conversion is almost flat, which is not surprising since in these cases the BIE is formed in its $|\pm X_{\mathrm{BIE}}\rangle$ eigenstates that do not evolve in time. Therefore, it is nearly impossible to obtain φ^0 from these measurements. However, since B polarized conversion transforms $|\pm X_{\mathrm{DE}}\rangle$ to $|\mp Y_{\mathrm{BIE}}\rangle$, which are coherent superpositions of the BIE eigenstates and thereby precess in time, the DCP is not flat, and φ^0 can be easily obtained. For $|\pm Y_{\mathrm{DE}}\rangle$ initializations, B converts $|\pm Y_{\mathrm{DE}}\rangle$ to $|\mp X_{\mathrm{BIE}}\rangle$, so the DCP signal is flat, while H converts $|\pm Y_{\mathrm{DE}}\rangle$ to $|\pm Y_{\mathrm{BIE}}\rangle$, so the DCP is not flat. For $|\pm Z_{\mathrm{DE}}\rangle$ initializations, the DCPs for both conversions are similar because in both cases $|\pm Z_{\mathrm{DE}}\rangle$ is converted to $|\pm Z_{BiE}\rangle$.

For each DE initialization, we determine the state by fitting the measured DCP curves of Fig. 6 for both H and B conversions to the model of Eq. (12). We note that only three fitting parameters, $[S_X^0, S_Y^0, S_Z^0]$, are used to fit four time-resolved DCP(t) curves for each DE preparation. Table I summarizes the best fitted tomography parameters that we obtained together with the BIE's characteristic times. Figure 7(a) displays the tomographic results on the DE Bloch sphere. Color-matched ovals in Fig. 7(a) represent one standard deviation of the experimental uncertainty of the measured states, while color-matched arrows represent the six initialized states. The length of the arrows represents the degree of polarization of each initialization, as independently measured to be 0.82, due to the finite efficiency of the optical depletion [48].

Finally, we show in Fig. 7(b) the 4×4 $\overleftrightarrow{M}$ matrix which maps the initialized DE state, represented by a 2×2 density matrix $\hat{\rho}_{\mathrm{init}}$, to the DE state density matrix that we obtain by
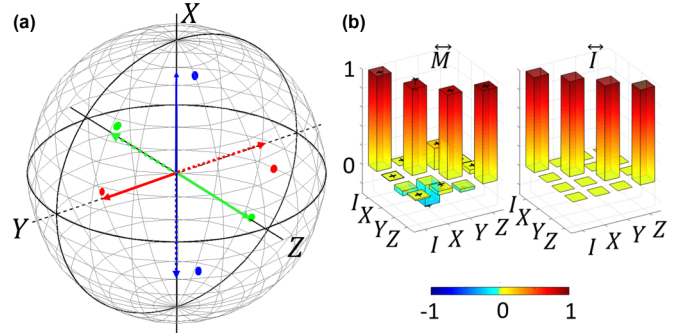

FIG. 7. (a) DE Bloch sphere, representing the initialized and measured states. Blue, red, and green arrows represent $|\pm X_{\mathrm{DE}}\rangle$, $|\pm Y_{\mathrm{DE}}\rangle$, and $|\pm Z_{\mathrm{DE}}\rangle$ DE initializations. The polarization degree is only 0.82 due to the finite efficiency of the optical depletion. The color-matched spots represent the tomographically measured states for each initialization. The spot's volume represents one standard deviation of the measurement uncertainty. (b) Matrix representation $\overleftrightarrow{M}$ of the state tomography measurement map. $\overleftrightarrow{M}$ is a 4×4 positive-definite and trace-preserving map that maps an initialized state (corrected for the 0.82 initialization) into the measured one. Error bars represent one standard deviation of the map's uncertainty. The fidelity of the measured physical map to the identity map [also shown in (b)] is 0.94 ± 0.02.

state tomography $\hat{\rho}_{\mathrm{tomog}}$,

$$\hat{\rho}_{\mathrm{tomog}} = \overleftrightarrow{M} \cdot \hat{\rho}_{\mathrm{init}}.$$

We obtain the $\overleftrightarrow{M}$ matrix from our measurements by finding the most probable positive and trace-preserving (physical) matrix that maps the six initial DE states to the measured ones in a procedure similar to the one described in Ref. [38]. The matrix that we obtain deviates from the expected 4×4 identity matrix $\overleftrightarrow{I}$, also shown in Fig. 7(b) for comparison. A fidelity of 0.94 ± 0.02 [50] quantifies the similarity between $\overleftrightarrow{M}$ and $\overleftrightarrow{I}$. We attribute this deviation to the calibration accuracy of our liquid-crystal variable retarder based polarization analyzers [30].

In summary, we demonstrated an all-optical measurement method for full state tomography of electronic spin qubits confined in semiconductor nanostructures. While previous methods require the spin to be a part of an optical Λ system, our method is more general since it relies on an optical Π system, typical of long-lived confined electronic spins, such as conduction-band electrons, valence-band holes, and dark excitons. The ability to perform full state tomography on electronic spins this way is essential for scaling up hybrid spin-multiphoton graph states [51], thereby constituting important step towards realizations of quantum information based technologies.

ACKNOWLEDGMENTS

[1] D. Loss and D. P. DiVincenzo, Phys. Rev. A **57**, 120 (1998).

[2] D. P. DiVincenzo, Fortschr. Phys. **48**, 771 (2000).

[3] B. E. Kane, Nature (London) **393**, 133 (1998).

[4] I. Bloch, Nature (London) **453**, 1016 (2008).

[5] J. Clarke and F. K. Wilhelm, Nature (London) **453**, 1031 (2008).

[6] R. Hanson and D. D. Awschalom, Nature (London) **453**, 1043 (2008).

[7] H. J. Kimble, Nature (London) **453**, 1023 (2008).

[8] A. Imamoglu, D. D. Awschalom, G. Burkard, D. P. DiVincenzo, D. Loss, M. Sherwin, and A. Small, Phys. Rev. Lett. **83**, 4204 (1999).

[9] N. Sangouard, C. Simon, H. de Riedmatten, and N. Gisin, Rev. Mod. Phys. **83**, 33 (2011).

[10] A. C. Johnson, J. R. Petta, J. M. Taylor, A. Yacoby, M. D. Lukin, C. M. Marcus, M. P. Hanson, and A. C. Gossard, Nature (London) **435**, 925 (2005).

[11] R. Blatt and D. Wineland, Nature (London) **453**, 1008 (2008).

[12] K. Saeedi, S. Simmons, J. Z. Salvail, P. Dluhy, H. Riemann, N. V. Abrosimov, P. Becker, H.-J. Pohl, J. J. L. Morton, and M. L. W. Thewalt, Science **342**, 830 (2013).

[13] D. Cogan, O. Kenneth, N. H. Lindner, G. Peniakov, C. Hopfmann, D. Dalacu, P. J. Poole, P. Hawrylak, and D. Gershoni, Phys. Rev. X **8**, 041050 (2018).

[14] R. Winik, D. Cogan, Y. Don, I. Schwartz, L. Gantz, E. R. Schmidgall, N. Livneh, R. Rapaport, E. Buks, and D. Gershoni, Phys. Rev. B **95**, 235435 (2017).

[15] X.-L. Wang, Y.-H. Luo, H.-L. Huang, M.-C. Chen, Z.-E. Su, C. Liu, C. Chen, W. Li, Y.-Q. Fang, X. Jiang, J. Zhang, L. Li, N.-L. Liu, C.-Y. Lu, and J.-W. Pan, Phys. Rev. Lett. **120**, 260502 (2018).

[16] A. J. Ramsay, S. J. Boyle, R. S. Kolodka, J. B. B. Oliveira, J. Skiba-Szymanska, H. Y. Liu, M. Hopkinson, A. M. Fox, and M. S. Skolnick, Phys. Rev. Lett. **100**, 197401 (2008).

[17] D. Heiss, V. Jovanov, M. Bichler, G. Abstreiter, and J. J. Finley, Phys. Rev. B **77**, 235442 (2008).

[18] H. Kosaka, T. Inagaki, Y. Rikitake, H. Imamura, Y. Mitsumori, and K. Edamatsu, Nature (London) **457**, 702 (2009).

[19] A. Morello, J. J. Pla, F. A. Zwanenburg, K. W. Chan, K. Y. Tan, H. Huebl, M. Möttönen, C. D. Nugroho, C. Yang, J. A. van Donkelaar, A. D. C. Alves, D. N. Jamieson, C. C. Escott, L. C. L. Hollenberg, R. G. Clark, and A. S. Dzurak, Nature (London) **467**, 687 (2010).

[20] P. Neumann, J. Beck, M. Steiner, F. Rempp, H. Fedder, P. R. Hemmer, J. Wrachtrup, and F. Jelezko, Science **329**, 542 (2010).

[21] J. J. Pla, K. Y. Tan, J. P. Dehollain, W. H. Lim, J. J. L. Morton, F. A. Zwanenburg, D. N. Jamieson, A. S. Dzurak, and A. Morello, Nature (London) **496**, 334 (2013).

[22] T. Nakajima, M. R. Delbecq, T. Otsuka, P. Stano, S. Amaha, J. Yoneda, A. Noiri, K. Kawasaki, K. Takeda, G. Allison, A. Ludwig, A. D. Wieck, D. Loss, and S. Tarucha, Phys. Rev. Lett. **119**, 017701 (2017).

[23] Y. Benny, S. Khatsevich, Y. Kodriano, E. Poem, R. Presman, D. Galushko, P. M. Petroff, and D. Gershoni, Phys. Rev. Lett. **106**, 040504 (2011).

[24] Y. Kodriano, I. Schwartz, E. Poem, Y. Benny, R. Presman, T. A. Truong, P. M. Petroff, and D. Gershoni, Phys. Rev. B **85**, 241304(R) (2012).

[25] M. Kroutvar, Y. Ducommun, D. Heiss, M. Bichler, D. Schuh, G. Abstreiter, and J. J. Finley, Nature (London) **432**, 81 (2004).

[26] D. Brunner, B. D. Gerardot, P. A. Dalgarno, G. Wüst, K. Karrai, N. G. Stoltz, P. M. Petroff, and R. J. Warburton, Science **325**, 70 (2009).

[27] K. De Greve, P. L. McMahon, D. Press, T. D. Ladd, D. Bisping, C. Schneider, M. Kamp, L. Worschech, S. Höfling, A. Forchel, and Y. Yamamoto, Nat. Phys. **7**, 872 (2011).

[28] E. Poem, Y. Kodriano, C. Tradonsky, N. H. Lindner, B. D. Gerardot, P. M. Petroff, and D. Gershoni, Nat. Phys. **6**, 993 (2010).

[29] I. Schwartz, E. R. Schmidgall, L. Gantz, D. Cogan, E. Bordo, Y. Don, M. Zielinski, and D. Gershoni, Phys. Rev. X **5**, 011009 (2015).

[30] I. Schwartz, D. Cogan, E. R. Schmidgall, L. Gantz, Y. Don, M. Zieliński, and D. Gershoni, Phys. Rev. B **92**, 201201(R) (2015).

[31] K. De Greve, P. L. McMahon, L. Yu, J. S. Pelc, C. Jones, C. M. Natarajan, N. Y. Kim, E. Abe, S. Maier, C. Schneider, M. Kamp, S. Höfling, R. H. Hadfield, A. Forchel, M. M. Fejer, and Y. Yamamoto, Nat. Commun. **4**, 3228 (2013).

[32] E. Togan, Y. Chu, A. S. Trifonov, L. Jiang, J. Maze, L. Childress, M. V. G. Dutt, A. S. Sørensen, P. R. Hemmer, A. S. Zibrov, and M. D. Lukin, Nature (London) **466**, 730 (2010).

[33] W. B. Gao, P. Fallahi, E. Togan, J. Miguel-Sanchez, and A. Imamoglu, Nature (London) **491**, 426 (2012).

[34] K. De Greve, L. Yu, P. L. McMahon, J. S. Pelc, C. M. Natarajan, N. Y. Kim, E. Abe, S. Maier, C. Schneider, M. Kamp, S. Höfling, R. H. Hadfield, A. Forchel, M. M. Fejer, and Y. Yamamoto, Nature (London) **491**, 421 (2012).

[35] J. R. Schaibley, A. P. Burgers, G. A. McCracken, L.-M. Duan, P. R. Berman, D. G. Steel, A. S. Bracker, D. Gammon, and L. J. Sham, Phys. Rev. Lett. **110**, 167401 (2013).

[36] N. H. Lindner and T. Rudolph, Phys. Rev. Lett. **103**, 113602 (2009).

[37] S. E. Economou, N. Lindner, and T. Rudolph, Phys. Rev. Lett. **105**, 093601 (2010).

[38] I. Schwartz, D. Cogan, E. R. Schmidgall, Y. Don, L. Gantz, O. Kenneth, N. H. Lindner, and D. Gershoni, Science **354**, 434 (2016).

[39] M. Bayer, G. Ortner, O. Stern, A. Kuther, A. A. Gorbunov, A. Forchel, P. Hawrylak, S. Fafard, K. Hinzer, T. L. Reinecke, S. N. Walck, J. P. Reithmaier, F. Klopf, and F. Schäfer, Phys. Rev. B **65**, 195315 (2002).

[40] E. L. Ivchenko, *Optical Spectroscopy of Semiconductor Nanostructures* (Alpha Science International, Ltd., 2005).

[41] M. Atature, Science **312**, 551 (2006).

[42] B. D. Gerardot, D. Brunner, P. A. Dalgarno, P. Öhberg, S. Seidl, M. Kroner, K. Karrai, N. G. Stoltz, P. M. Petroff, and R. J. Warburton, Nature (London) **451**, 441 (2008).

[43] G. Ramon, U. Mizrahi, N. Akopian, S. Braitbart, D. Gershoni, T. L. Reinecke, B. D. Gerardot, and P. M. Petroff, Phys. Rev. B **73**, 205330 (2006).

[44] J. McFarlane, P. A. Dalgarno, B. D. Gerardot, R. H. Hadfield, R. J. Warburton, K. Karrai, A. Badolato, and P. M. Petroff, Appl. Phys. Lett. **94**, 093113 (2009).

[45] Y. Benny, Y. Kodriano, E. Poem, S. Khatsevitch, D. Gershoni, and P. M. Petroff, Phys. Rev. B **84**, 075473 (2011).

[46] Ş. C. Bădescu and T. L. Reinecke, Phys. Rev. B **75**, 041309(R) (2007).

[47] A. Bechtold, D. Rauch, F. Li, T. Simmet, P.-L. Ardelt, A. Regler, K. Muller, N. A. Sinitsyn, and J. J. Finley, Nat. Phys. **11**, 1005 (2015).

[48] E. R. Schmidgall, I. Schwartz, D. Cogan, L. Gantz, T. Heindel, S. Reitzenstein, and D. Gershoni, Appl. Phys. Lett. **106**, 193101 (2015).

[49] Y. Benny, Y. Kodriano, E. Poem, D. Gershoni, T. A. Truong, and P. M. Petroff, Phys. Rev. B **86**, 085306 (2012).

[50] R. Jozsa, J. Mod. Opt. **41**, 2315 (1994).

[51] D. Buterakos, E. Barnes, and S. E. Economou, Phys. Rev. X **7**, 041023 (2017).